 doi:10.20944/preprints202107.0366.v1

Article

The Optical Coherence Tomography and Raman spectroscopy for sensing of the bone demineralization process

Maciej Głowacki, Aleksandra Kamińska, Marcin Gnyba, Jerzy Pluciński, and Marcin R. Strąkowski *

Department of Metrology and Optoelectronics, Faculty of Electronics, Telecommunications and Informatics, Gdańsk University of Technology, 11/12 G. Narutowicza Str., 80-233 Gdańsk, Poland.

* Correspondence: marcin.strakowski@pg.edu.pl; Tel.: +48 58 347 2642

Abstract: Aim of the presented research was to develop an optical sensing system to investigate the demineralization process of the bones. Optical measurement techniques are widely used and increasingly adapted in biological and biomedical applications due to their non-destructive nature and safety. Optical examination of the bone condition could facilitate clinical trials and improve the safety of patients. The authors used a set of complementary methods: polarization-sensitive optical coherence tomography (PS-OCT) and Raman spectroscopy. To stimulate the process of demineralization and gradual removal of the hydroxyapatite, the test samples of chicken bones were placed into 10% acetic acid. Measurements were carried out in two series. The first one took two weeks with data acquired every day. In the second series, the measurements were made during one day at an hourly interval (after 1, 2, 3, 5, 7, 10, and 24 hours). Raman spectroscopy was used to evaluate the disappearance of the hydroxyapatite. The relation between the content of hydroxyapatite and images recorded using OCT was analyzed and discussed. Moreover, the polarization properties of the bones have been evaluated. Based on OCT images, the retardation angles of the bones have been calculated. This work presents a preliminary study on the mechanism of bone demineralization and confirms the potential of the applied optical methods.

Keywords: bones; polarization-sensitive optical coherence tomography; Raman spectroscopy

1. Introduction

Bones in human organisms play several important roles. They form a skeleton – a living structure, capable of growth, adaptation, and repair. The human skeleton throughout its lifetime adjusts its size and internal structure to the constantly changing biomechanical conditions. Due to their mechanical strength, the bones play a protective role for the various organs (e.g., the skull protects the brain and ribs protect the heart and lungs). The second, at least equally important role of the bones, resulting from their mechanical tensile strength, compressive strength, and fracture toughness, is the supporting role (e.g., bones allow the body to control the shape and to move using muscles and joints). Apart from the "mechanical roles" of the bones, they are an important reservoir of Ca^{2+} ions. In the bone tissue the fixed processes of distribution and biochemical and structural components renewing occur. Osteoblasts take a part in the formation process and bone regeneration. During ossification, they create trabecular forms making up the skeletal system. Osteoclasts are involved during the dissolution process and superstructure bone. The macro bone construction represents two forms: cancellous tissue and compact one. The last one creates an oriented structure composed of lamellae (collagen fibers) with a clear orientation.

Bone is a complex and not easily classifiable composite of organic substances and mineral compounds entangled on a nanostructured level [1–3]. The basic unit of the organic component of the bone is the type I collagen molecule, which is a long (300 nm) and thin (1.5 nm in diameter) protein composed of a triple helix. Repeated segments of five collagen molecules arranged parallel to each other in one plane at equal intervals of

 doi:10.20944/preprints202107.0366.v1

0.24 nm, with every subsequent molecule being lowered from the previous one by 67 nm, form a microfibril, which is presented in Figure 1 [2,4,5]. The C termini of the succeeding segments are separated from the N termini of the preceding ones by a distance (gap) of 36 nm [4]. A bunch of alternatively arranged microfibrils forms a fibril, which in turn is an element of a tissue fiber [4,6]. Since the neighboring microfibrils are aligned, the gaps present in their structure create continuous channels [2,4]. The presence of both collagen and hydroxyapatite in bones in approximately 1 to 3 weight ratios makes the bones very strong and flexible at the same time.

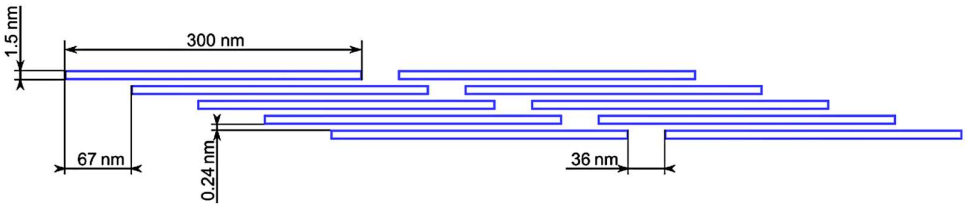

Figure 1. Arrangement of collagen in the microfibril. The diameters of the proteins and the 0.24 nm spaces between the molecules are disproportionately large for the illustration.

The inorganic template of the bone is composed of hydroxyapatite, which predominantly occurs as a non-stoichiometric mineral of a hexagonal crystal system [7,8]. Hydroxyapatite is known to nucleate and grow within the gap channels, creating platelets of varying sizes and spatial orientations [3,4]. The crystals are uniaxially oriented along the long axis of the collagen molecules [2,3]. A significant amount of the mineral is also reported to exist in the extrafibrillar space [4]. The hydroxyapatite is a factor that introduces considerable irregularity to the otherwise hierarchical and highly organized structure of the collagen fibrils.

Diverse types of bones bear the closest resemblance to each other on the nanostructured level [9]. Making the optical properties of the samples dependent on the changes in their nanostructure enables partial reduction of the impact of differences between specimens.

On ossification, two major changes: osteoclastogenesis and osteoblastogenesis take place [10,11]. The balance that exists between these processes is responsible for the process of bone remodeling. During bone remodeling, the process of bone loss is closely coupled to the reconstruction process, which determines the proper functioning of the skeleton. Any imbalance between remodeling processes may cause serious disease. Lower bone mineralization may be due to age (not all bones are fully mineralized after birth), diseases (among which osteoporosis is best known), or injuries. Significant bone weakness leads to, for example, fractures or deformities. In some rare cases, excessive bone mineralization may occur, manifesting itself as a decrease in its elasticity. One of the main factors of the healthy state of bone tissues is the proper management of calcium as a form of hydroxyapatite.

In the clinical diagnosis, the healthiness of the bone is mainly examined using computed tomography (CT) with the Hounsfield method for tissue hardness evaluation. In bone regeneration, the monitoring of tissue growth is a key element, which determines the success of treatment. Because of the high negative influence of X-ray radiation on a human body, the measurements are usually carried out with respect to the principal rule of ALARA (As Low As Reasonably Achievable). However, due to the need to reduce testing CT of the negative impact of ionizing radiation on living organisms (from 5 to 100 times greater than conventional radiographs of the same area of the body) defers to the time of evaluation of bone tissue on average for the period of 6 months and up to 9 months, which significantly extends the time of implant treatment.

The purpose of the study is to determine whether or not bone mineralization or demineralization can be estimated by means of complementary optical methods. As the

 doi:10.20944/preprints202107.0366.v1

bones are highly scattering media, the authors decided to use an optical coherent tomography (OCT, pioneered by David Huang, James G. Fujimoto, and co-workers in 1991 [12]. It is an optical measurement technique used for the investigation of a wide range of scattering materials. The OCT enables surface and subsurface examination of different types of materials to be performed in a non-contact and non-destructive way. With the aid of OCT, one can analyze the depth structure of investigated materials with a measurement resolution of a few micrometers, high sensitivity, and dynamic range. Nowadays, the advantages of OCT make it applied in medical treatments, especially in ophthalmology, dermatology, stomatology, and endoscopy, and also in industry and science. The high application potential of OCT makes it a valuable tool for researchers from many areas. The OCT measurements are based on the selective detection of the light backscattered from the particular scattering points located inside the investigated object, which is needed for 2D and 3D tomography imaging. It means that using OCT the backscattered light can be gathered with high spatial resolution. To perform such measurements, the OCT uses low-coherence interferometry (LCI). The LCI, also known as white light interferometry (WLI), is an attractive measurement method offering high measurement resolution, high sensitivity, and measurement speed. Since both hydroxyapatite and collagen fibers are birefringent, it has been decided to use polarization-sensitive optical coherent tomography (PS-OCT), which allows simultaneous measurements of the scattering properties of bone and its polarization properties.

PS-OCT has so far been used in an investigation of hydroxyapatite-containing tissue specimens, namely teeth (tooth enamel is an anisotropic weakly scattering medium that changed the state of polarization of back-scattering optical radiation [9,13–16]) as well as collagen-containing tissues (e.g., skin [17,18], articular cartilage [19–22], meniscus [21], tendons [23], tumor [24,25], and atherosclerotic plaques [26] or coronary plaque [27] in blood vessels).

Raman spectroscopy was used as a complementary method to verify the PS-OCT measurements. The method is based on the illumination of the sample by a laser beam and spectral analysis of the inelastically scattered light. Interaction between the excitation light and oscillating molecular bonds results in the appearance of the spectral lines which correspond to the distribution of oscillatory levels, which is unique to a particular material (e.g., hydroxyapatite). Thus, Raman spectroscopy provides crucial information about the molecular composition of investigated materials. The intensity of the Raman line is proportional to the concentration of oscillators (bonds) in an analyzed volume of the material, thus reducing the content of the substance (reduces the intensity of this line). Raman spectroscopy has been widely used for biomaterials investigation. For this purpose, IR laser excitation is commonly used as this wavelength range enables significant reduction of fluorescence signal which creates strong optical background which interferes with Raman signal acquisition and processing. A significant advantage of the Raman measurement is the use of signals in the VIS-NIR spectral range. It enables the use of fiber-optic probes which simplifies the coupling of the optical measurement system to the object of investigation as well as improves the safety of the measurements [28–30].

Because the bones are highly scattering media, the use of PS-OCT or Raman spectroscopy systems for their examination, for example, for estimation of their demineralization, could have been a much more difficult task. In this study, for ethical reasons, bones of animals having similar properties to humans, which was previously intended for human consumption, were only used. Conclusions from the conducted research, due to the similarity of bone structure, may be extended to human bones. Therefore, the presented research results can be used in the future in the development of diagnostic methods assessing changes in the degree of bone mineralization caused by natural, disease, or injury factors during bone regeneration or fusion. These tests can also be the basis for the assessment of bone formation processes, e.g., around implanted hip or elbow joints, etc.

2. Experimental procedure

2.1. Sample preparation and investigation procedure

Extracted chicken humeri have been used for the optical analysis of the demineralization process. Separate sets of the samples were prepared for measurements by PS-OCT and Raman spectroscopy. Diaphyses of the bones were thoroughly cleansed of muscle tissues while tendons and articular cartilage were removed from the epiphyses. To ensure repeatability of the scanned area, for every sample a thin transverse notch has been made in the middle of the diaphysis. The bones have always been measured from the notch toward the distal epiphysis. For PS-OCT examination the objects have been additionally leveled. The appearance of the prepared humerus with a marked scanning area is presented in Figure 2.

Figure 2. Extracted chicken humerus prepared for the reference OCT measurement. The green rectangle indicates the scanned region.

Reference measurements have been carried out with PS-OCT and Raman spectroscopy after the bones were rinsed with saline solution and dried in the open air. Subsequently, the samples were placed in 10% acetic acid to gradually remove hydroxyapatite from their structure. Two series of measurements have been carried out, each on a separate set of bones. The first group of the humeri was being examined during the first 24 hours of the demineralization, namely after 1 h, 2 h, 3 h, 5 h, 7 h, 10 h, and finally 24 h. The second set of samples has been investigated every 24 h for 2 weeks using polarization-sensitive optical coherence tomography and Raman spectroscopy. In this study the samples were labeled as B24h_OCT – the sample used in the 24-hours experiment for PS-OCT measurements, B24h_RS – the sample used in the 24-hours experiment for Raman spectroscopy, B14D_OCT – the sample used in 14-days experiment for PS-OCT measurements, B14D_RS – the sample used in 14-days experiment for Raman spectroscopy. The acetic acid greatly altered the mechanical properties of the samples. After 2 weeks of demineralization, the bones became flexible and could easily be bent.

2.2. PS-OCT and Raman spectroscopic measurement systems

PS-OCT measurements were carried out with the use of a PS-SS-OCT system with commercial laser swept source HSL-2000 by Santec. During each PS-OCT measurement 128 horizontal sections (B-scans) have been obtained for the single sample, with every image having been composed of 1024 axial scans (A-scans).

Raman spectroscopic system utilizes NIR excitation wavelength to reduce the influence of fluorescence and other optical background signals. The Raman system is based on axial transmissive spectrograph and fiber-optic probe from the pre-commercial Raman system Ramstas developed by the VTT — Technical Research Center of Finland [28,29]. The system also uses a diode laser coupled to an optical fiber. Power on the sample was limited to reduce the risk of its thermal damage. Collected scattered radiation is filtered to remove laser wavelength and transmitted to the spectrograph and TE-cooled CCD camera Andor BV-401.

Detailed features of the measurement systems used in this study are presented in Table 1.

 doi:10.20944/preprints202107.0366.v1

Table 1. Features of the PS-OCT system and the Raman spectrometer.

PS-OCT system		Raman spectrometer	
Item	**Value**	**Item**	**Value**
Light source type	Diode laser – 20 kHz swept source	Light source type	Diode laser – CW mode
Average output power	10 mW	Average output power	100 mW
Central wavelength	1320 nm	Central wavelength	830 nm
Wavelength range	140 nm	Raman spectral range	Stokes band – 200–2000 cm^{-1}
Longitudinal resolution	12 μm	Spectral resolution	8 cm^{-1}
Lateral resolution	15 μm	Spectrograph	Axial transmissive setup with a holographic transmission grating
Frame rate	> 4 fps	Detector	TE-cooled CCD array – 1024 columns, –50°C
Depth imaging range	7 mm	Optical system	Fiber optics probe – working distance of 5 cm
Transverse imaging range	10 mm		

3. Measurements and data processing

3.1. Polarization-sensitive optical coherence tomography measurements (PS-OCT)

All measurements of the evaluated samples of the chicken humerus were made with the aid of polarization-sensitive analysis (PS) applied to OCT. The PS analysis expands the OCT imaging by delivering information about the birefringence of the tested sample. These data are given in the form of a retardation angle, which can be understood as a phase shift between ordinary and extraordinary optical beams in the birefringent medium. An example of PS-OCT measurements of the chicken humerus is shown in Figure 3.

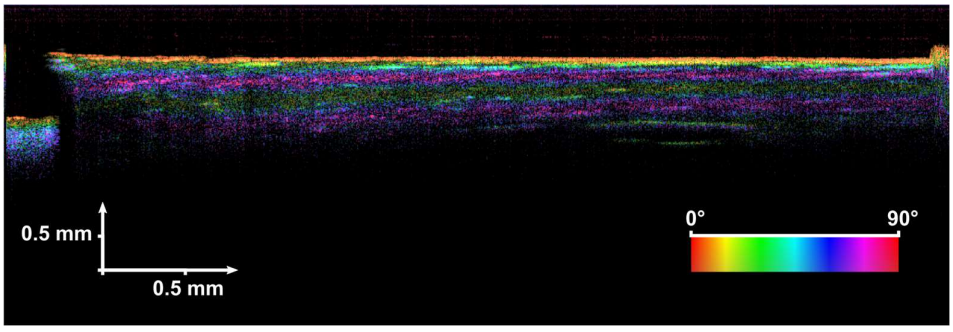

Figure 3. An example of PS-OCT imaging of the chicken humerus after 1 day on harsh environment exposure (sample B14D_OCT).

Standard OCT imaging usually expresses the changes of the backscattered light intensity as a grayscale cross-sectional image. Here, the retardation angle has been added creating colorful multimodal OCT images. The intensity (value) of the image pixels corresponds to the level of backscattered light at a logarithmic scale. Whereas, the value of retardation angle is coded by the color of the pixels (hue) according to the scale represented by the color bar.

Preprints (www.preprints.org) | NOT PEER-REVIEWED | Posted: 16 July 2021 doi:10.20944/preprints202107.0366.v1

The PS-OCT system, which was utilized in the experiment, estimates the retardation angle based on the Jones formalism, therefore, its value varies from 0 to $\pi/2$ (0 to 90 degrees). For the continuous increase of the retardation value with depth, the retardation angle becomes a periodic function, which can be seen as regular color stripes in Figure 3.

Following the experimental procedure, described in section 2, 22 PS-OCT images were collected and processed for further analysis: 7 for sample B24h_OCT (taken in the first 24 hours) and 15 for sample B14D_OCT (taken in the first 14 days). A representative set of the measurement results, which express the observed trends and support the conclusions, have been shown in Figure 4.

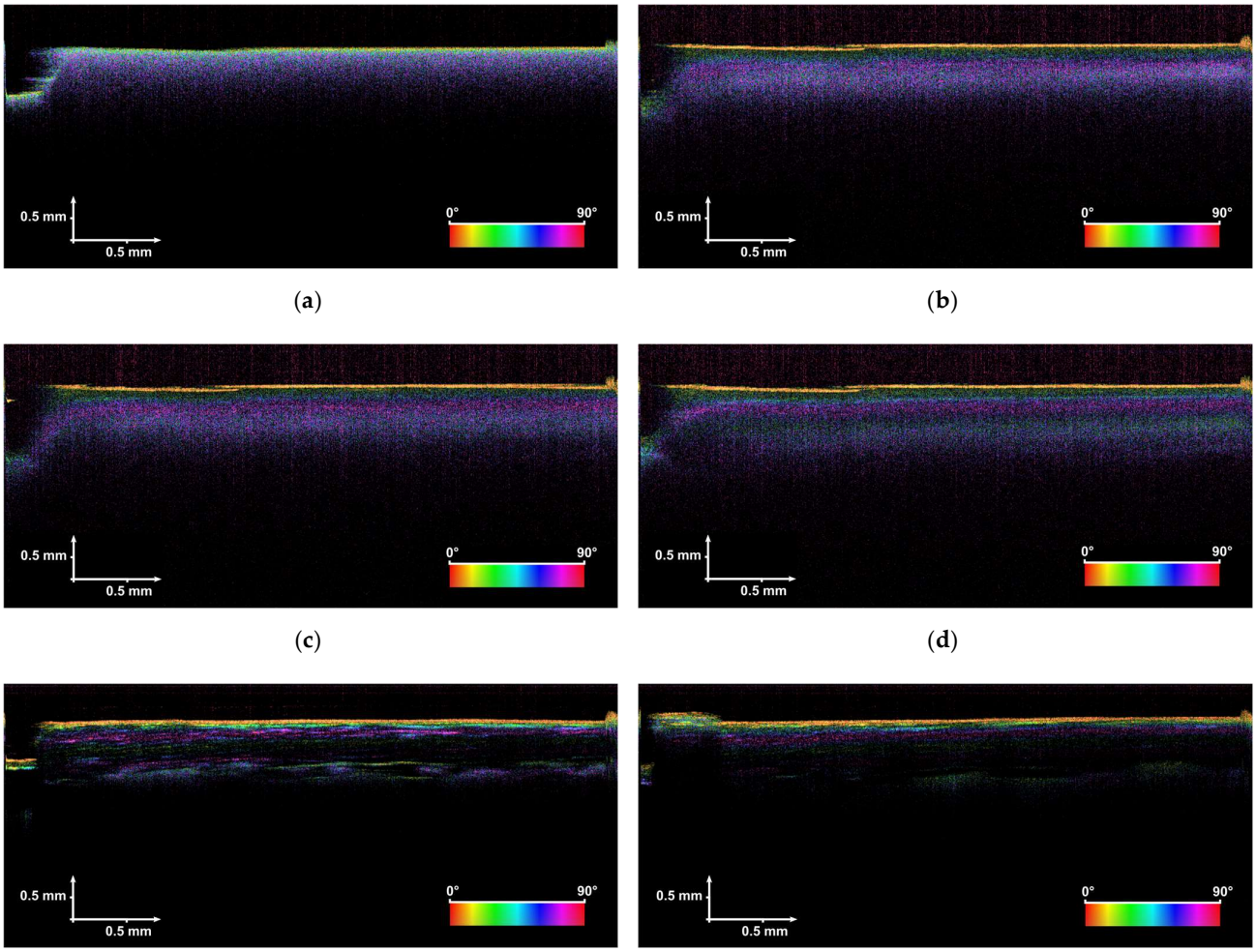

Figure 4. PS-OCT images of the tested bone taken in the first 24 hours (sample B24h_OCT – figures (**a**)–(**d**) and 14 days (sample B14D_OCT – figures (**e**)–(**f**); (**a**) the image taken at the beginning of the experiment (the bone has not been put under the acetic acid influence), (**b**) after 1 hour; (**c**) after 3 hours; (**d**) after 24 hours, (**e**) after 7 days; (**f**) after 14 days.

The first attempt at the analysis was based on subjective evaluation of the PS-OCT cross-sectional images. Following, the two main trends are seen. Firstly, sample exposure to acetic acid reduces the optical scattering and absorption effects inside the tested bone. This has been observed for both B24h_OCT and B14D_OCT samples as a lower level of backscattered light from the bone inner structure in exposure time. To underline this conclusion one should compare the images in Figure 4. The PS-OCT image, labeled as (a), was taken at the beginning of the experiment for the bone, which has not been affected by the acid. Comparing this PS-OCT image with the (b), (c), and (d) the lower intensity of

 doi:10.20944/preprints202107.0366.v1

backscattered light from the sample subsurface structure and higher penetration depth can be noticed. This phenomenon increase especially after a longer exposure time (longer than 1 or 2 days), which is expressed by analyzing PS-OCT images (e) and (f) in Figure 4. Some valuable conclusions can be derived from the polarization-sensitive measurements. The first PS-OCT image in the series of B24h_OCT measurements expresses a random change in the retardation angle (the sample has not been influenced by acid yet), which suggests the light depolarizing nature of the evaluated structure. After 24 hours of bone exposure to the acid, regular color stripes can be seen, which leads to the conclusion that the sample exhibited some birefringent effects. This and the scattering phenomena in bones have been proceeded to quantitative analysis, described in the next session.

3.2. Analysis of the backscattered light intensity

Among the others, the intensity of backscattered optical signal depends on the Fresnel reflections, and scattering and absorption coefficients of the evaluated tissue. The relation between scattering features of the tissues and recorded OCT signals (A-scans) were studied in [31] and [32]. Analyzing PS-OCT images, which have been taken after long tissue exposure to acetic acid – see images (e) and (f) in Figure 4, a low level of backscattered light intensity (dark areas) between surface and subsurface interfaces can be observed. This phenomenon is a consequence of low tissue scattering and absorption in this particular case and leads us to expand the investigation by observing their changes in exposure time. Analyzing the scattering and absorption independently is difficult especially using OCT methods. Therefore, the quantitative evaluation was based on the extinction coefficient, which represents both effects.

The OCT recorded signal covers information about back-reflected and backscattered light at the surface and inside the evaluated sample. The first component refers to the reflection at the boundary between the sample and surrounding medium (e.g., the air), and between the layers composing the device under tests, which is described by the Fresnel equations. The back-reflected signal occurs as rapid rise and fall of the value of the A-scan (single line of depth-resolved OCT scan). Whereas, the slower changes at the A-scan are related to the backscattered effects of the scanning light beam. The rate of the A-scan slope may indicate the regions, at which the back-reflection or backscattering becomes a dominant effect. This has been expressed as an example presented in Figure 5.

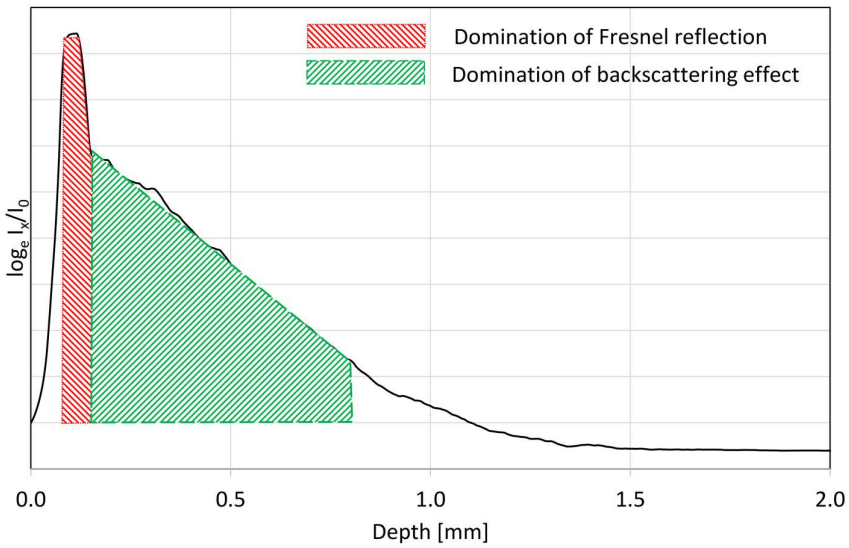

Figure 5. An example of OCT A-scan, at which the regions of Fresnel reflection and backscattering domination were indicated; I_x – the intensity of backscattered/back-reflected optical radiation, I_0 – reference intensity, usually the intensity of the incoming light beam.

 doi:10.20944/preprints202107.0366.v1

Following the outcomes from [31], the OCT A-scan, as a function of depth, is described as the compound of an optical source point spread function (PSF) and Beer's law. Due to the exponential character of backscattered light intensity, the extinction coefficient is calculated directly from the A-scan as a slope ratio of its natural logarithm.

The raw data from the OCT system are in the form of A-scans in the logarithmic scale (dB). The data processing started from defining the region of interests (ROI) at OCT image, covering the B-scan from the marking notch toward the distal epiphysis, and limited at depth to the backscattered light intensity drop by 20 dB. Afterward, all A-scans were adjusted to the point of light reflection from the surface of the evaluated sample, which clears out the tilt of the OCT image. Following, all A-scans inside the selected ROI were recalculated to linear scale and averaged together. At last, the averaged plot was recalculated again to the scale with a natural logarithm as a base. The extinction coefficient was estimated from the slope of the plot at the region, at which the light backscattering effects are dominant over the Fresnel reflection. The above procedure has been applied to the measurement results obtained for samples B24h_OCT and B14D_OCT. The values of extinction coefficient as a function of time of exposure to the acetic acid were presented in Figure 6 and 7.

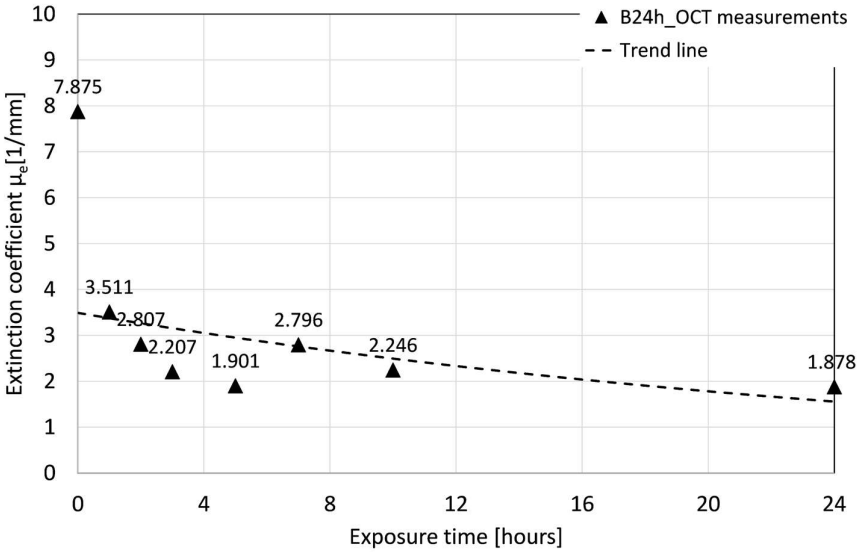

Figure 6. The average value of the extinction coefficient measured for the first 24 hours of the experiment – sample B24h_OCT.

Preprints (www.preprints.org) | NOT PEER-REVIEWED | Posted: 16 July 2021 doi:10.20944/preprints202107.0366.v1

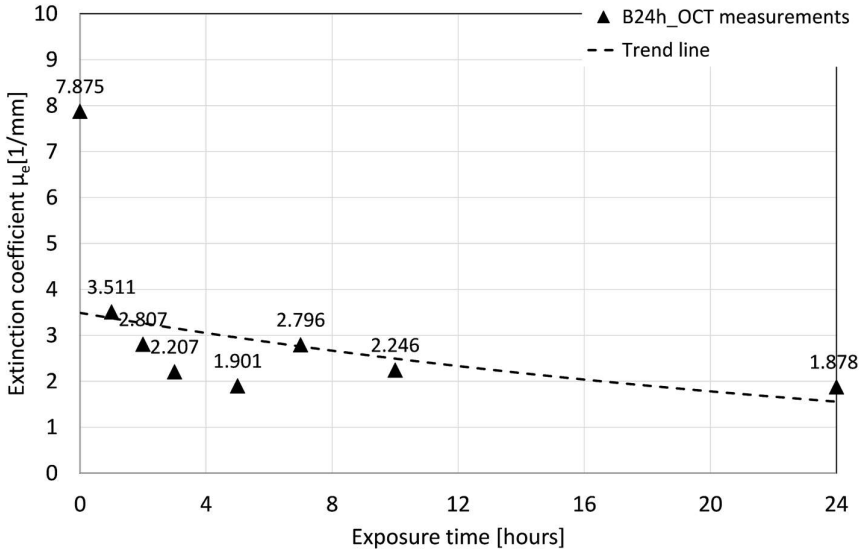

Figure 7. The average value of the extinction coefficient measured for a longer period – sample B14D_OCT.

The presented quantitative data express the dynamic change in the light scattering of the bones during the demineralization process, which is stimulated by exposure to the acid. After few days of the test, the bone sample has become almost transparent for the NIR radiation used in the experiment. The highest drop of the extinction coefficient has been observed after the second hour of the acid influence on the bone.

3.3. Polarization-sensitive analysis in the bones evaluation

In the utilized PS-OCT system, the polarization-sensitive measurement data are delivered in the form of depth-resolved wrapped function of a retardation angle with a periodicity of π. The retardation angle exposes the phase shift between linear orthogonal components of polarized light guided through a birefringent medium. Due to the birefringent nature of collagen and hydroxyapatite, this effect has been expected in our observation. In this particular case, birefringence (Δn) defined as the difference between refractive indexes for both polarization orthogonal components (known as ordinary and extraordinary rays) is the best approach to express the polarization effects in the bones. The Δn can be calculated easily from the derivative of the retardation angle function. This has been shown in Figure 8.

Preprints (www.preprints.org) | NOT PEER-REVIEWED | Posted: 16 July 2021 doi:10.20944/preprints202107.0366.v1

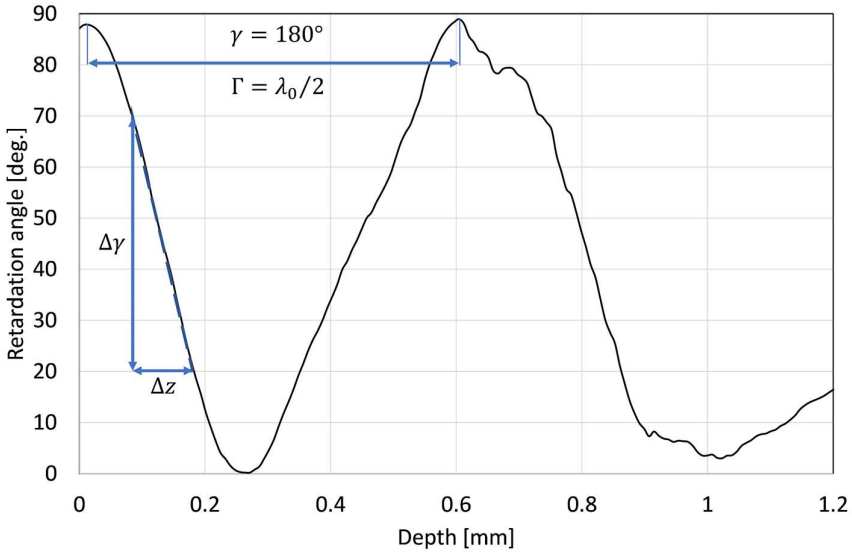

Figure 8. An example of a plot of retardation angle taken for a single A-scan.

The birefringence Δn is also referred to the retardation provided by the tested sample at the specific geometrical path z, which is expressed as:

$$\Delta n = \Gamma / z \tag{1}$$

or

$$\Delta n = (\gamma \cdot \lambda_0)/(2\pi \cdot z), \tag{2}$$

where: γ is the retardation angle, Γ is the retardation (expressed in length units) as a delay between polarization orthogonal components at a specific geometrical path z, and λ_0 is the central wavelength of the scanning beam (1320 nm for the utilized PS-OCT system).

Depending on the plot of retardation angle, two different approaches were applied. If the two neighboring maxima or minima were recognized, the Δn has been calculated based on equation (1), where provided retardation was equal to half of the central wavelength and z was the distance between these maxima. Otherwise, the birefringence estimation has been done by analyzing the slope of the plot, which has been presented in Figure 8 as a dashed line. In this case, the Δn has been calculated as:

$$\Delta n = (\Delta\gamma \cdot \lambda_0)/(2\pi \cdot \Delta z) \tag{3}$$

where $\Delta\gamma$ is the retardation angle change over the path length Δz.

The raw data were in the form of a two-dimensional map of retardation angle, which covers the cross-sectional OCT image inside the ROI selected for the "Analysis of the backscattered light intensity", described in the previous subsection. The data processing starts from eliminating bright and dark spots (locally extremely high and low values) using a median filter. As previously, each line (A-scan) of the retardation map has been adjusted according to the surface of the tested bone. Afterward, all values were averaged in the lateral direction (towards the distal epiphysis) to obtain the smooth depth-resolved function of the retardation angle. At last, the birefringence as the Δn has been calculated based on the procedure described above. The change in birefringence as a function of time of exposure to acid is presented in Figure 9 and 10.

Preprints (www.preprints.org) | NOT PEER-REVIEWED | Posted: 16 July 2021 doi:10.20944/preprints202107.0366.v1

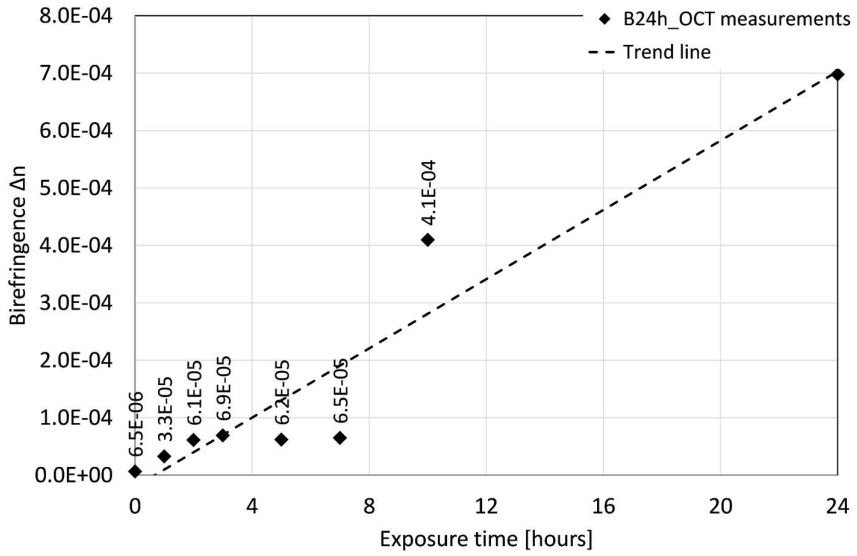

Figure 9. The average value of birefringence of the chicken humerus recorded for the first 24 hours of exposure to acid – sample B24h_OCT.

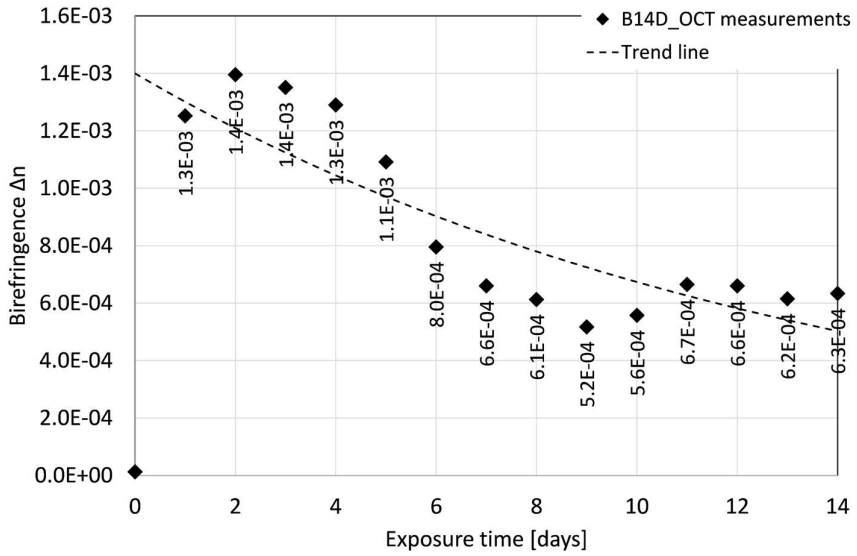

Figure 10. The average value of birefringence of the chicken humerus recorded for 14 days of exposure to acid – sample B14D_OCT.

At a beginning of the experiment, both tested samples (B24h_OCT and B14D_OCT) present a high ability to depolarize the scanning light beam, which occurred as a random change of the value of retardation angle observed at PS-OCT B-scans (Figure 4a) and closed to 0 value of calculated birefringence Δn. After a short time of exposure to the acid (about 1 hour), the bones exhibited some birefringent-like behavior, which has been seen as a rising value of Δn. For the next hours, the Δn has been rising rapidly. This process has taken about two days from the beginning of the experiment. Afterward, the fall of birefringence has been observed and after about eight days its value became stable.

3.4. Raman Spectroscopy

Raman spectra were processed with the use of OriginLab OriginPro software. Selected Raman spectra recorded during the experiment taking 24 hours (sample B24h_RS) and 14 days (sample B14D_RS) are shown in Figure 11. The main Raman band at 967 cm-

 doi:10.20944/preprints202107.0366.v1

^{1} has been already reported in the literature [33,34]. It is assigned to $\nu(PO_3)$ symmetric stretching of hydroxyapatite. As the strongest band assigned to hydroxyapatite, it was used as a marker for quantitative estimation of demineralization of the bone which is the result of its interaction with the acetic acid.

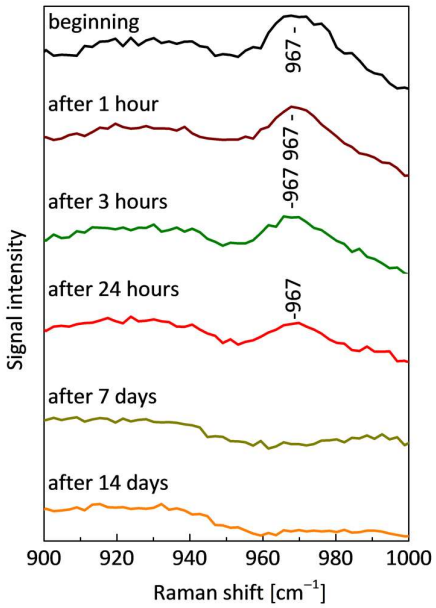

Figure 11. The average value of the extinction coefficient measured for the first 24 hours of the experiment – sample B24h_OCT.

Before the analysis, an optical offset was removed from the Raman spectra by polynomial approximation and subtraction. For quantitative analysis, the integral intensity (area) of the band was calculated with the use of the Lorenz function. The result of the integral intensity calculation was divided by the intensity value for a different Raman shift value that should have remained constant during the experiment (760 cm^{-1} was selected as an example) to overcome the small defocusing effect caused by the complex surface of the sample. Then results were normalized in relation to the values determined for initial measurements in order to quantify the disappearance of hydroxyapatite in the investigated area of the bone. Results are shown in Figure 12.

The time courses of normalized intensity changes of the Raman bands at 967 cm^{-1} are in good agreement with the results of the OCT investigation. As a result of the integration of the bone with the acid the intensity of the line assigned to hydroxyapatite quickly decreases. This indicates the demineralization of the sample, caused by decomposition and/or flushing out the hydroxyapatite. Despite the small differences in the speed of this process between two samples (the sample evaluated during the 24 hours and the second one measured for 14 days), caused by individual variation, one can observe that it was the most intense during the first day (decrease to about 20-40% of initial values), especially during the first three hours. After about 5-7 days the Raman signal assigned to the hydroxyapatite cannot be noticed. The character of changes is best approximated by the exponential function.

 doi:10.20944/preprints202107.0366.v1

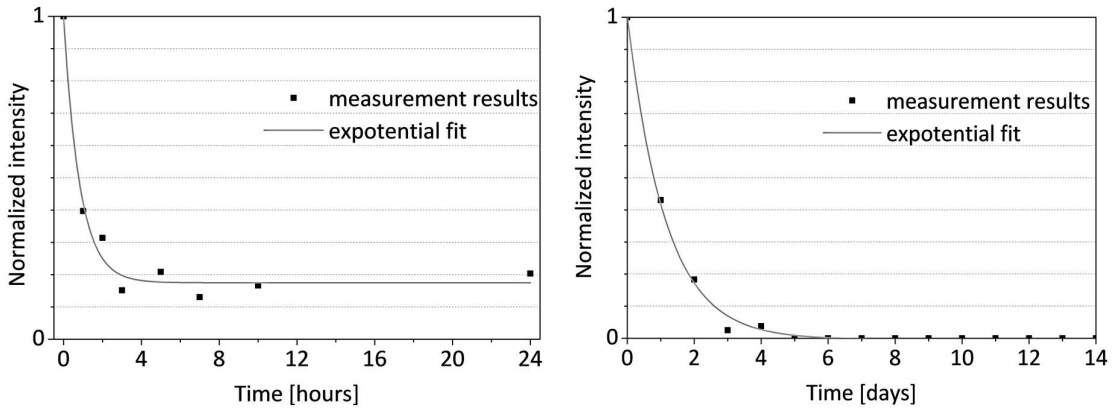

Figure 12. The time courses of normalized intensity changes of the Raman band at 967 cm^{-1} during: (**a**) sample B24h_RS – 24-hour experiment, (**b**) sample B14D_RS – 14-days experiment.

4. Discussion

All PS-OCT and Raman observations were performed with reference to the sample evaluated at the beginning of the experiment (Figure 4a). For this sample, the measurements were taken before it had been influenced by the acetic acid. In this case, the obtained PS-OCT result expresses a typical tomographic image for highly-scattering, isotropic medium: i) lower penetration of the scanning beam in-depth comparing to the other PS-OCT measurement results, ii) high backscattered signal from subsurface layers, iii) retardation angle changing randomly. In comparison with the reference data, the other PS-OCT images exhibit some birefringent features of the sample with the reduced volume of hydroxyapatite. Moreover, the sample becomes more transparent in the NIR radiation range, which has been shown by observing the distinctly lower intensity of backscattered light.

These conclusions are confirmed by the analysis of the change in birefringence (Figure 9 and 10) and the extinction coefficient (Figure 8 and 9) of the evaluated sample in the first 24 hours and for the longer period of 14 days. For the evaluation of sample scattering abilities, the extinction coefficient μ_e becomes a key factor. Referring to the experiment, the highest μ_e has been noticed for the first measurements at the beginning, where the evaluated sample highly scattered the scanning beam. Afterward, the μ_e has been dropping, which might be explained by the optical clearance of the sample by acetic acid infiltration. Due to its optical high-scattering features [35], the healthy bone exhibits high values of extinction coefficient. A noticeable decrease in the μ_e caused by lower scattering was observed, which correlates with OCT images and Raman spectroscopic measurements. The rapid fall of the μ_e values occurred in the first hour. After 3 hours the process was stabilized and its dynamics became much lower than in the first 3 hours. After seven days the bones became almost completely transparent for the scanning optical beam.

The composition of hydroxyapatite and collagen fibrils makes the bone very durable, as well as highly scattering and depolarizing. However, both components have birefringent features, therefore, monitoring of the birefringence (Δn) has been carried out. At the beginning (the zero time) the value of Δn was low. It meant that the sample did not exhibit birefringence features or is highly scattering, which depolarized the scanning beam. After putting the sample under the acetic acid influence the significant growth of the birefringence has been observed. Referring to Figure 9 and 10, the phenomenon was observed for the first 3 hours of the hydroxyapatite reduction process and has been continued for the next days. After the second day of the experiment, the birefringence reached its maximum and became slowly falling to reach its stable value after the 8^{th} day of the experiment.

 doi:10.20944/preprints202107.0366.v1

The birefringence (Δn) and the extinction coefficient (μ_e) are sensitive to the changes in bone structure and its biochemical composition. With a gradual removal of the inorganic matrix (hydroxyapatite), monitored with the aid of Raman spectroscopy, the μ_e has decreased, while, Δn has designated significant growth.

The comparison of the results recorded with the OCT method and Raman spectroscopy, which are characterized by good timing, indicates the possibility of explaining changes in the optical parameters of the bones through changes in its internal structure – removal of the hydroxyapatite. The process during the first days was very intense especially in the layer of the near-surface bone. Removal of the hydroxyapatite skeleton, which due to its orientation (see Figure 1) disturbs bone birefringence, causes the material to become more birefringent due to the parallel orientation of collagen fibers. This process is accompanied by an increase in the penetration depth of the measurement signals and birefringence changes observed by the PS-OCT method and some Raman signal fluctuations, which results from the fact that the measurement signals began to contain a composition of deeper layers, in which there was still residual hydroxyapatite.

After about two weeks, the sample became soft, which additionally confirms the hypothesis about the demineralization processes taking place, and at the same time shows that after this time they covered the entire volume of the examined bone.

This confirms the possibility of using bimodal PS-OCT and Raman measurements for early determination of changes associated with bone demineralization or comparative study of their mineralization level.

5. Conclusions

This study expresses the possibilities to assess the degree of hard tissue demineralization. The use of the dedicated PS-OCT and Raman system equipped with IR sources for the investigation of bones enables the acquisition of sufficient intensity signals and reduced impact of optical interferences. According to obtained results, the strong correlation between the level of the hydroxyapatite reduction in the bones monitored with the aid of Raman spectroscopy and the polarization-sensitive optical coherence tomography imaging can be observed. Likewise, the dynamic of the bone demineralization process can be measured successfully by both PS-OCT and Raman spectroscopy. This PS-OCT method may have application potential in the monitoring of resorption and regeneration process of the bones as well as early detection of pathological changes. It can be used during bone recuperation after, e.g., bone injury, surgery, or implant application. This report presents the preliminary results, which discover the capabilities of the PS-OCT for bone diagnosis. More research work is needed for quantitative data recovery from PS-OCT imaging to make this technique useful in clinical practice. Moreover, the problem of the bones imaging through skin and muscles using PS-OCT has not been solved. All measurements presented in this report were performed *ex vivo*. For now, direct access to the surface of the bone is required, which becomes a key problem to be overcome. Obviously, this method can be used during surgery, where easy access to the bone is maintained. Also, there are some studies, in which the admittance to the evaluated hard tissue is provided by the optical interface through the implant [36]. However, further studies on optical interfaces to the bones, as well as better optical signal acquisition and recovery are needed. Moreover, for the wide application of the optical method in the investigation of tissues and other biological materials, it is necessary to compare and optimize the performance of different PS-OCT and Raman measurement systems [3740].

Author Contributions: Conceptualization, M.Gł., A.K., M.S., J.P., and M.Gn.; methodology, M.S. and M.Gn.; sample preparation, M.Gł.; OCT measurements, M.Gł., J.P., and A.K.; OCT data analysis, M.S.; Raman measurements and data analysis, M.Gn.; formal analysis, M.S. and J.P.; resources, J.P. and M.Gn.; data curation, M.S. and M.Gn.; writing—original draft preparation, M.Gł. and A.K.; writing—review and editing, M.S. and J.P.; supervision, J.P.; All authors have read and agreed to the published version of the manuscript.

Funding: This research was funded by the Faculty of Electronics, Telecommunications and Informatics, Gdańsk University of Technology.

Acknowledgments: Technical support from the VTT – Technical Research Centre of Finland (components of the Raman spectroscopic system) is gratefully acknowledged.

Conflicts of Interest: The authors declare no conflict of interest. The funders had no role in the design of the study; in the collection, analyses, or interpretation of data; in the writing of the manuscript, or in the decision to publish the results.

References

1. Eliaz, N.; Metoki, N. Calcium Phosphate Bioceramics: A Review of Their History, Structure, Properties, Coating Technologies and Biomedical Applications. *Materials* **2017**, *10*, 334, 1–104. https://dx.doi.org/10.3390/ma10040334
2. Olszta, M.J.; Cheng, X.; Jee, S.S.; Kumar, R.; Kim, Y.Y.; Kaufman, M.J.; Douglas, E.P.; Gower, L.B. Bone structure and formation: A new perspective. *Mater. Sci. Eng., R* **2007**, *58*, 77–116. https://dx.doi.org/10.1016/j.mser.2007.05.001
3. Rubin, M.A.; Jasiuk, I.; Taylor, J.; Rubin, J.; Ganey, T.; Apkarian, R.P. TEM analysis of the nanostructure of normal and osteoporotic human trabecular bone. *Bone* **2003**, *33*, 270–282. https://dx.doi.org/10.1016/s8756-3282(03)00194-7
4. Alexander, B.; Daulton, T.L.; Genin, G.M.; Lipner, J.; Pasteris, J.D.; Wopenka, B.; Thomopoulos, S. The nanometre-scale physiology of bone: steric modelling and scanning transmission electron microscopy of collagen–mineral structure. *J. R. Soc. Interface* **2012**, *9*, 1774–1786. https://dx.doi.org/10.1098/rsif.2011.0880
5. Wegst, U.G.K.; Bai, H.; Saiz, E.; Tomsia, A.P.; Ritchie, R.O. Bioinspired structural materials. *Nat. Mater.* **2015**, *14*, 23–36. https://dx.doi.org/10.1038/nmat4089
6. Orgel, J.P.R.O.; Irving, T.C.; Miller, A.; Wess, T.J. Microfibrillar structure of type I collagen *in situ*. *PNAS* **2006**, *103*, 9001–9005. https://dx.doi.org/10.1073/pnas.0502718103
7. Haverty, D.; Tofail, S.A.M.; Stanton, K.T.; McMonagle, J.B. Structure and stability of hydroxyapatite: Density functional calculation and Rietveld analysis. *Phys. Rev. B: Condens. Matter* **2005**, *71*, 094103. https://dx.doi.org/10.1103/PhysRevB.71.094103
8. Leventouri, T. Synthetic and biological hydroxyapatites: Crystal structure questions. *Biomaterials* **2006**, *27*, 3339–3342. https://dx.doi.org/10.1016/j.biomaterials.2006.02.021
9. Fried, D.; Xie, J.; Shafi, S.; Featherstone, J.D.; Breunig, T.M.; Le, C. Imaging caries lesions and lesion progression with polarization sensitive optical coherence tomography. *J. Biomed. Opt.* **2002**, *7*, 618–627. https://dx.doi.org/10.1117/1.1509752
10. Tortora, G.J.; Derrickson, B. Principles of Anatomy and Physiology, 15th ed.; John Wiley & Sons: Hoboken, NJ, USA, 2017; 171–193.
11. Stern, P.H. (Ed.) *Bone Regulators and Osteoporosis Therapy*; Springer Nature Switzerland AG: Cham, Switzerland, 2020. https://dx.doi.org/10.1007/978-3-030-57378-2
12. Huang, D.; Swanson, E.A.; Lin, C.P.; Schuman, J.S.; Stinson, W.G.; Chang, W.; Hee, M.R.; Flotte, T.; Gregory, K.; Puliafito, C.A.; Optical coherence tomography. *Science* **1991**, *254*, 1178–1181. https://dx.doi.org/10.1126/science.1957169
13. Louie, T.M.; Jones, R.S.; Sarma, A.V.; Fried, D. Selective removal of composite sealants with near ultraviolet laser pulses of nanosecond duration. *J. Biomed. Opt.* **2005**, *10*, 014001, 1–6. https://dx.doi.org/10.1117/1.1854676
14. de Melo, L.S.; de Araujo, R.E.; Freitas, A.Z.; Zezell, D.; Vieira, N.D.; Girkin, J.; Hall, A.; Carvalho, M.T.; Gomes, A.S. Evaluation of enamel dental restoration interface by optical coherence tomography. *J. Biomed. Opt.* **2005**, *10*, 064027, 1–5. https://dx.doi.org/10.1117/1.2141617
15. Sinescu, C.; Negrutiu, M.L.; Todea, C.; Balabuc, C.; Filip, L.; Rominu, R.; Bradu, A.; Hughes, M.; Podoleanu, A.G. Quality assessment of dental treatments using en-face optical coherence tomography. *J. Biomed. Opt.* **2008**, *13*, 054065, 1–8. https://dx.doi.org/10.1117/1.2992593
16. Piao, D.; Zhu, Q.; Dutta, N.K.; Yan, S.; Otis, L.L. Cancellation of coherent artifacts in optical coherence tomography imaging. *Appl. Opt.* **2001**, *40*, 5124–5131. https://dx.doi.org/10.1364/AO.40.005124
17. Pierce, M.C.; Strasswimmer, J.; Parke, B.H.; Cense, B.; de Boer, J.F. Birefringence measurements in human skin using polarization-sensitive optical coherence tomography. *J. Biomed. Opt.* **2004**, *9*, 287–291. https://dx.doi.org/10.1117/1.1645797
18. Pircher, M.; Goetzinger, E.; Leitgeb, R.; Hitzenberger, C.K. Three dimensional polarization sensitive OCT of human skin in vivo. *Opt. Express* **2004**, *12*, 3236–3244. https://dx.doi.org/10.1364/OPEX.12.003236
19. Xie, T.; Xia, Y.; Guo, S.; Hoover, P.; Chen, Z.; Peavy, G.M. Topographical variations in the polarization sensitivity of articular cartilage as determined by polarization-sensitive optical coherence tomography and polarized light microscopy. *J. Biomed. Opt.* **2008**, *13*, 054034, 1–11. https://dx.doi.org/10.1117/1.2976422
20. Youn, J.-I.; Vargas, G.; Wong, B.J.F.; Milner, T.E. Depth-resolved phase retardation measurements for laser-assisted non-ablative cartilage reshaping. *Phys. Med. Biol.* **2005,** *50*, 1937–1950. https://dx.doi.org/10.1088/0031-9155/50/9/001
21. Xie, T.; Guo, S.; Zhang, J.; Chen, Z.; Peavy, G.M. Use of polarization-sensitive optical coherence tomography to determine the directional polarization sensitivity of articular cartilage and meniscus. *J. Biomed. Opt.* **2006**, *11*, 064001, 1–8. https://dx.doi.org/10.1117/1.2397574

22. Ugryumova, N.; Attenburrow, D.P.; Winlove, C.P.; Matcher, S.J. The collagen structure of equine articular cartilage, characterized using polarization-sensitive optical coherence tomography. *J. Phys. D: Appl. Phys.* **2005**, *38*, 2612–2619. https://dx.doi.org/10.1088/0022-3727/38/15/012
23. Real, E.; Icardo J.M.; Fernández-Barreras, G.; Revuelta, J.M.; Díez, M.C.; Pontón, A.; Gutiérrez J.F.; Higuera, J.M.L.; Conde O.M. Identification of Human Pathological Mitral Chordae Tendineae Using Polarization-sensitive Optical Coherence Tomography. *Sensors* **2019**, *19*, 543, 1–12. https://dx.doi.org/10.3390/s19030543
24. Baumann, B. Polarization Sensitive Optical Coherence Tomography: A Review of Technology and Applications. *Appl. Sci.* **2017**, *7*, 474, 1–34. https://dx.doi.org/10.3390/app7050474
25. de Boer, J.F.; Hitzenberger, C.K.; Yasuno, Y. Polarization sensitive optical coherence tomography – a review [Invited]. *Biomed. Opt. Express* **2017**, *8*, 1838–1873. https://dx.doi.org/10.1364/BOE.8.001838
26. Giattina, S.D.; Courtney, B.K.; Herz, P.R.; Harman, M.; Shortkroff, S.; Stamper, D.L.; Liu, B.; Fujimoto, J.G.; Brezinski, M.E. Assessment of coronary plaque collagen with polarization sensitive optical coherence tomography (PS-OCT). *Int. J. Cardol.* **2006**, *107*, 400–409. https://dx.doi.org/10.1016/j.ijcard.2005.11.036
27. Nadkarni, S.K.; Bouma, B.E.; de Boer, J.; Tearney, G.J. Evaluation of collagen in atherosclerotic plaques: the use of two coherent laser-based imaging methods. *Lasers Med. Sci.* **2009**, *24*, 439–445. https://dx.doi.org/10.1007/s10103-007-0535-x
28. Niemelä, P.; Suhonen, J. Rugged Fiber-Optic Raman Probe for Process Monitoring Applications. *Appl. Spectrosc.* **2001**, *55*, 1337–1340. https://dx.doi.org/10.1366/0003702011953694
29. Niemelä, P.; Sumen, J.; Suhonen, J., Dual-laser CCD-Raman spectrometer applied to on-line measurement of paper coating paste. *Proc. SPIE Int. Soc. Opt. Eng.* **2005**, *5826*, 406–411. https://dx.doi.org/10.1117/12.623477
30. Keränen, M.; Maaninen, A.; Gnyba, M.; Maaninen, T. Spectroscopic studies of a ring opening process between epoxy- and aminosilanes and imine formation reactions in aqueous solutions. *J. Sol-Gel. Sci. Technol.* **2018**, *87*, 725–733. https://dx.doi.org/10.1007/s10971-018-4758-z
31. Yang, Y.; Wang, T.; Biswal, N.C.; Wang, X.; Sanders, M.; Brewer, M.; Zhu, Q. Optical scattering coefficient estimated by optical coherence tomography correlates with collagen content in ovarian tissue. *J. Biomed. Opt.* **2011**, *16*, 090504, 1–4. https://dx.doi.org/10.1117/1.3625247
32. Andersen, P.E.; Jørgensen, T.M. Modeling Light–Tissue Interaction in Optical Coherence Tomography Systems. In *Optical Coherence Tomography*, 2nd ed.; Drexler, W., Fujimoto, J.G., Eds.; Springer: Cham, Switzerland, 2015; Volume 1, pp. 95–140.
33. Koutsopoulos, S. Synthesis and characterization of hydroxyapatite crystals: A review study on the analytical methods. *J. Biomed. Mater. Res.* **2002**, *62*, 600–612. https://dx.doi.org/10.1002/jbm.10280
34. Mandair, G.S.; Morris, M.D. Contributions of Raman spectroscopy to the understanding of bone strength. *BoneKEy Reports* **2015**, *4*, 620, 1–8. https://dx.doi.org/10.1038/bonekey.2014.115
35. Bashkatov, A.N.; Genina, E.A.; Kochubey, V.I.; Tuchin, V.V. Optical properties of human cranial bone in the spectral range from 800 to 2000 nm. *Proc. SPIE Int. Soc. Opt. Eng.* **2006,** *6163*, 616310, 1–11. https://dx.doi.org/10.1117/12.697305
36. Weber, J.R.; Baribeau, F.; Grenier, P.; Émond, F.; Dubois, S.; Duchesne, F.; Girard, M.; Pope, T.; Gallant, P.; Mermut, O.; Moghadam, H.G. Towards a bimodal proximity sensor for in situ neurovascular bundle detection during dental implant surgery. *Biomed. Opt. Express* **2014**, *5*, 16–30. https://dx.doi.org/10.1364/BOE.5.000016
37. Strąkowski, M.; Pluciński, J.; Kosmowski, B.B. Polarization sensitive optical coherence tomography with spectroscopic analysis. *Acta Phys. Pol. A* **2011**, *120*, 785–788. https://dx.doi.org/10.12693/APhysPolA.120.785
38. Kraszewski, M.; Strąkowski, M.; Pluciński, J.; Kosmowski, B. Spectral measurement of birefringence using particle swarm optimization analysis. Appl. Opt. 2015, 54, 76–84. https://dx.doi.org/10.1364/AO.54.000076
39. Wang, J.; Chaney, E.J.; Aksamitiene, E.; Marjanovic, M.; Boppart S.A. Compressive sensing for polarization sensitive optical coherence tomography. *J. Phys. D: Appl. Phys.* **2021**, *54*, 294005, https://dx.doi.org/10.1088/1361-6463/abf958
40. Guo, S.; Beleites, C.; Neugebauer, U.; Abalde-Cela, S.; Afseth, N.K.; Alsamad, F.; Anand, S.; Araujo-Andrade, C.; Aškrabić, S.; Avci, E.; et. al. Comparability of Raman Spectroscopic Configurations: A Large Scale Cross-Laboratory Study. *Anal. Chem.* **2020**, *92*, 15745–15756. https://dx.doi.org/10.1021/acs.analchem.0c02696